

Astronomy & Astrophysics manuscript no.
(will be inserted by hand later)

Far-infrared mapping of the starburst galaxy NGC 253 with ISOPHOT. *

M. Radovich¹, J. Kahanpää² and D. Lemke³

¹ Osservatorio Astronomico di Capodimonte, via Moiariello 16, I-80131 Napoli, Italy
e-mail: radovich@na.astro.it

² Observatory, University of Helsinki, PL 14, 00014 Helsingin yliopisto, Finland
e-mail: jere.kahanpaa@helsinki.fi

³ Max-Planck-Institut für Astronomie, Königstuhl 17, D-69117 Heidelberg, Germany
e-mail: lemke@mpia-hd.mpg.de

Received xxx /Accepted xxx

Abstract. A 180 μm map and strip maps at 120 and 180 μm were obtained for the edge-on starburst galaxy NGC 253 with ISOPHOT, the photometer on board the *Infrared Space Observatory*. We compare these observations with those obtained by IRAS at 60 μm and 100 μm and derive the far-infrared spectral energy distribution at different locations in the galaxy. There is evidence for the presence of cold dust ($T \leq 20$ K) both in the nucleus and in the disk. Extended emission dominated by cold dust is detected up to $\sim 15'$ (~ 10 kpc) along the major and minor axis; its spatial distribution is similar to that seen in the IRAS and ROSAT PSPC images. The emission along the minor axis is probably related to large-scale outflows of gas (superwinds) which originate in the nuclear starburst and maybe to star formation in the halo. The radial dependence of the dust temperature along the major axis is found using a radiative transfer code: we show that the dust scale length in the disk is $\sim 40\%$ larger than that of stars.

Key words. Infrared: galaxies - ISM: dust - galaxies: spiral - galaxies: ISM - galaxies: starburst - galaxies: NGC 253

1. Introduction

There is growing evidence (Trewhella et al. 2000) for the existence of two components in the dust distribution in galaxies, a spatially extended distribution of cold dust ($T < 20\text{K}$) and a warm dust ($T > 20\text{K}$) component concentrated in the disk, probably associated with star formation. The most direct evidence for the existence of the cold dust component has been provided by SCUBA and by ISOPHOT, the photometer on board the *Infrared Space Observatory* (ISO, Kessler et al. 1996), in particular thanks to the C200 detector. The cold dust may lie both along the disk, in which case the dust scale length may be higher than the stellar scale length by factors of 40% to 80% (Alton et al. 1998b) and vertically. If a massive nuclear starburst is present, supernovae forming there may drive the gas from the inner disk of the host galax-

ies to their halos, as first proposed by Chevalier & Clegg (1985) and later Heckman et al. (1990). Dust entrained in these outflows should enhance the far-infrared emission vertically to the disk; this effect should be most easily observed in edge-on galaxies.

NGC 253 is a nearby, almost edge-on barred spiral galaxy (De Vaucouleurs et al. 1991); we adopt a distance of 2.5 Mpc (Houghton et al. 1997), which gives a projected linear scale of 12 pc/arcsec. NGC 253 is one of the nearest galaxies showing evidence for a compact nuclear starburst (size ~ 100 pc, Dudley & Wynn-Williams 1999) which is partially responsible for its high far-infrared luminosity, $L_{\text{FIR}} \sim 2 \times 10^{10} L_{\odot}$. NGC 253 has been extensively observed in all spectral ranges (see e.g. Engelbracht et al. 1998 and Forbes et al. 2000). Still uncertain is the presence of a highly obscured AGN which would contribute some of the radio and X-ray emission, but none of the optical and infrared emission (Forbes et al. 2000).

Send offprint requests to: M. Radovich

* Based on observations with ISO, an ESA project with instruments funded by ESA Member States (especially the Principal Investigator countries: France, Germany, Netherlands and the United Kingdom) and with the participation of ISAS and NASA.

McCarthy et al. (1987) found along the minor axis an extended emission-line region associated with diffuse x-ray emission, over $\sim 15''$ in diameter: they identified this emission-line gas with cool dense clouds embedded in an outflowing wind of hot gas. Fabbiano (1988) found more

extended, low surface brightness X-ray emission extending along the minor axis out to $10'$ (NW) and $5'$ (SE). More recently, Dahlem et al. (1998) analyzed ROSAT PSPC and HRI and ASCA data and found a diffuse, hot soft X-ray halo with dimensions of 16×10 kpc and attributed it to the superwind. Pietsch et al. (2000) also investigated the extended X-ray emission from ROSAT HRI and PSPC data: they separated the total halo emission in a corona component which originates from the halo immediately above the disk (scale height ~ 1 kpc) and in an outer halo which extends to projected distances from the disk of 9 kpc and shows a horn-like structure. However, IRAS images of NGC 253 did not provide straightforward results. Rice (1993) and Alton et al. (1998a) presented high-resolution IRAS maps produced with the Maximum Correlation Method (MCM) technique; they concluded that spurious effects like detector hysteresis at 12 and $25 \mu\text{m}$ and emission reflected from the IRAS telescope spider at 60 and $100 \mu\text{m}$ mask low-level emission outside the disk. Alton et al. (1999) presented submillimeter images of the nuclear regions of NGC 253 obtained with SCUBA and found evidence for a dust outflow along the minor axis at $450 \mu\text{m}$ on a size $\leq 45''$.

In this paper we report the results of observations of NGC 253 obtained with ISOPHOT; available data and their processing are discussed in sec. 2. The investigation aims at:

1. Evaluating the far-infrared emission properties in different regions of the galaxy and look for evidence of the outflow in the FIR. To this purpose we combine the ISOPHOT $180 \mu\text{m}$ map with the IRAS maps (sec. 3): an estimate of dust temperatures and masses is obtained by fitting the so-obtained spectral energy distributions with a simple model (sum of two modified blackbodies).
2. Analyzing the radial dependence of the dust temperature using a radiative transfer code (sec. 4). FIR emission properties in the disk are compared to those derived from optical data, which are mainly related to the stellar component.

2. Observations and Data Reduction

NGC 253 was observed with ISOPHOT (Lemke et al. 1996) in the staring raster mode with the multi-filter Astronomical Observation Template PHT22 (Klaas et al. 1994) and the C200 detector. The staring raster mode is a sequence of staring observations on a two-dimensional ($M \times N$) regular grid which consists of a sequence of space-craft pointings. As given in Table 1, a map was obtained at $180 \mu\text{m}$ covering a $53' \times 26'$ field. The separation of the raster points was equal to the C200 array size ($180''$), which resulted in gaps between them. In addition, four strip ($N=1$) maps were performed in the 120 and $180 \mu\text{m}$ filters. They were oriented roughly along the minor axis of NGC 253 and centered on the nucleus and offset posi-

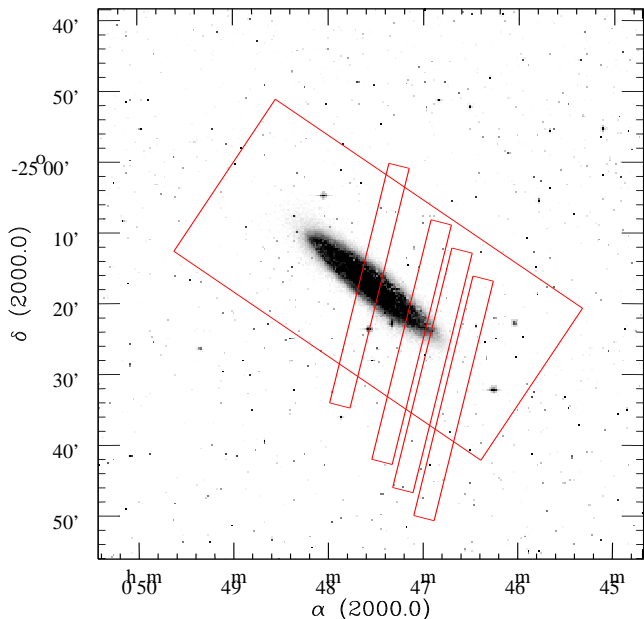


Fig. 1. The areas covered by ISOPHOT maps have been overlaid to J band image of NGC 253 from the Digitized Sky Survey, obtained using the SkyView survey analysis system.

tions of 10 , 15 and $20'$. The positions of the four maps are shown in Fig. 1.

The data reduction was performed using the ISOPHOT Interactive Analysis tool (PIA, version 7.2) together with the calibration data set V 4.0 (Laureijs et al. 1998): corrections were made for non-linearity effects of the electronics, disturbances by cosmic rays (deglitching) and signal dependence on the reset interval time. The flux calibration is based on measurements with the thermal fine calibration sources (FCS) on board: two FCS measurements were taken, one before and one after each observation in order to correct for changes in the detector responsivity. According to Klaas et al. (2000), ISOPHOT absolute calibration accuracies for extended sources observed in the staring raster mode are $\leq 25\%$. Saturation occurred in the nucleus both at 120 and $180 \mu\text{m}$; this could be at least partially recovered only in the $180 \mu\text{m}$ strip map including the destructive read-outs, which are usually discarded.

Our data were further processed using a series of procedures developed by Manfred Stickel at MPIA. A first set of procedures allowed to improve the flat field correction of the $180 \mu\text{m}$ map. A second set of procedures allowed to interpolate between the detector gaps changing the pixel size to $50''$ and to rotate the map; these procedures are based on the 'drizzle' algorithm (Fruchter & Hook 1997) implemented in IRAF. ISOPHOT maps of a point-like source (NGC 7027) at 120 and $200 \mu\text{m}$ were processed following the same procedure, in order to measure the size (FWHM) of the beam profile: in both cases we obtain $\text{FWHM} = 122''$.

Table 1. Log of the ISOPHOT observations. The position angle (PA) is from North to East. Offsets from the nucleus are given for the strip maps.

λ (μm)	$\frac{\lambda_c}{\Delta\lambda_c}$	offset	M	N	δM	δN	fov	PA	exp (s)
120	2.4	0	11	1	180''	0	35' x 3'	166°	960
120	2.4	10'	11	1	180''	0	35' x 3'	166°	960
120	2.4	15'	11	1	180''	0	35' x 3'	166°	960
120	2.4	20'	11	1	180''	0	35' x 3'	166°	960
180	2.6	0'	11	1	180''	0	35' x 3'	166°	960
180	2.6	10'	11	1	180''	0	35' x 3'	166°	960
180	2.6	15'	11	1	180''	0	35' x 3'	166°	960
180	2.6	20'	11	1	180''	0	35' x 3'	166°	960
180	2.6	8	17		180''	180''	26' x 53'	34°	4200

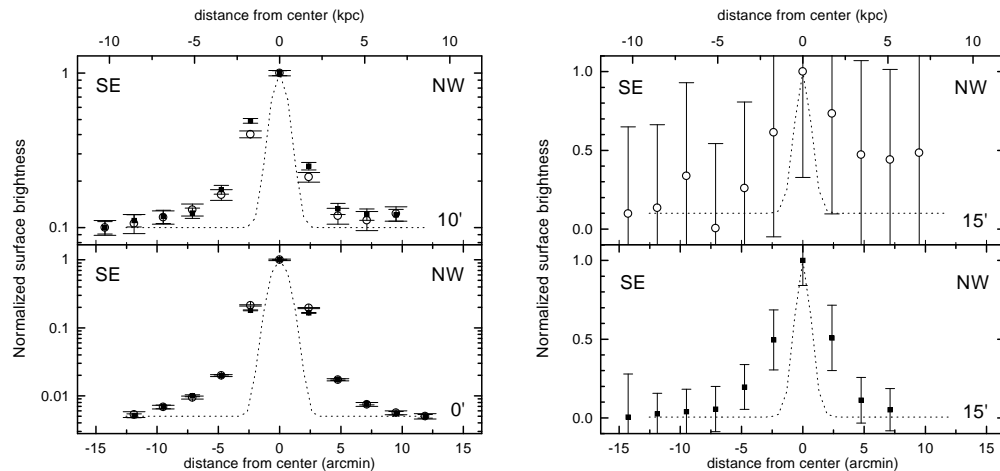


Fig. 2. Surface brightness profiles normalized to the peak brightness in the strip maps at $120\,\mu\text{m}$ (open circles) and $180\,\mu\text{m}$ (filled squares) at offsets of $0'$, $10'$ (left) and $15'$ (right). The lower limit has been chosen to emphasize the extended part of the emission; error bars are computed from the statistical uncertainties on measured surface brightnesses. The dashed line is the beam profile derived from ISOPHOT maps of a point-like source at 120 and $200\,\mu\text{m}$.

2.1. IRAS maps

IRAS images of NGC 253 processed with the High Resolution (HIRES) technique were obtained from the Infrared Processing and Analysis Center (IPAC). A detailed description of this technique was given by Rice (1993). We used the maps with twenty iterations, giving resolutions of $37\text{x}23''$ ($12\,\mu\text{m}$), $35\text{x}23''$ ($25\,\mu\text{m}$), $62\text{x}41''$ ($60\,\mu\text{m}$) and $98\text{x}80''$ ($100\,\mu\text{m}$).

The IRAS maps were convolved with a Gaussian function to the FWHM of the ISOPHOT beam profile at $200\,\mu\text{m}$ ($122''$) and registered to the ISOPHOT $180\,\mu\text{m}$ map using the coordinate information contained in the headers of the image files: the registration also included matching the pixel size in the maps. The reliability of the registration was checked by the coincidence of the surface brightness peak; the IRAS and ISOPHOT maps are compared in Fig. 3.

3. Mapping of the FIR emission

The surface brightness profiles in the strip maps show (see Fig. 2) that the emission is dominated by the strong nuclear source. However, extended emission is also present along the minor axis, in particular in the strip centered on the nucleus ($0'$ offset) where it may be detected within uncertainties to a distance $\sim 8'$ from the nucleus and with decreasing signal to $\sim 12'$. We define this emission as the ‘halo’ component, in addition to that detected along the major axis (‘disk’) and in the center (‘nucleus’). Along the major axis, emission is detected up to $15'$, where the data at $120\,\mu\text{m}$ are significantly noisier than at $180\,\mu\text{m}$; no emission above the background is detected in the $20'$ strip map. In order to measure the fluxes in these three components, we defined circular apertures at different positions in the galaxy (see Fig. 3 and Table 2) and computed the integrated fluxes from the background-subtracted IRAS and ISOPHOT maps.

The flux measured in the aperture centered on the nucleus is the sum of disk and nuclear emission. Due to the poor spatial resolution it was not possible to separate the

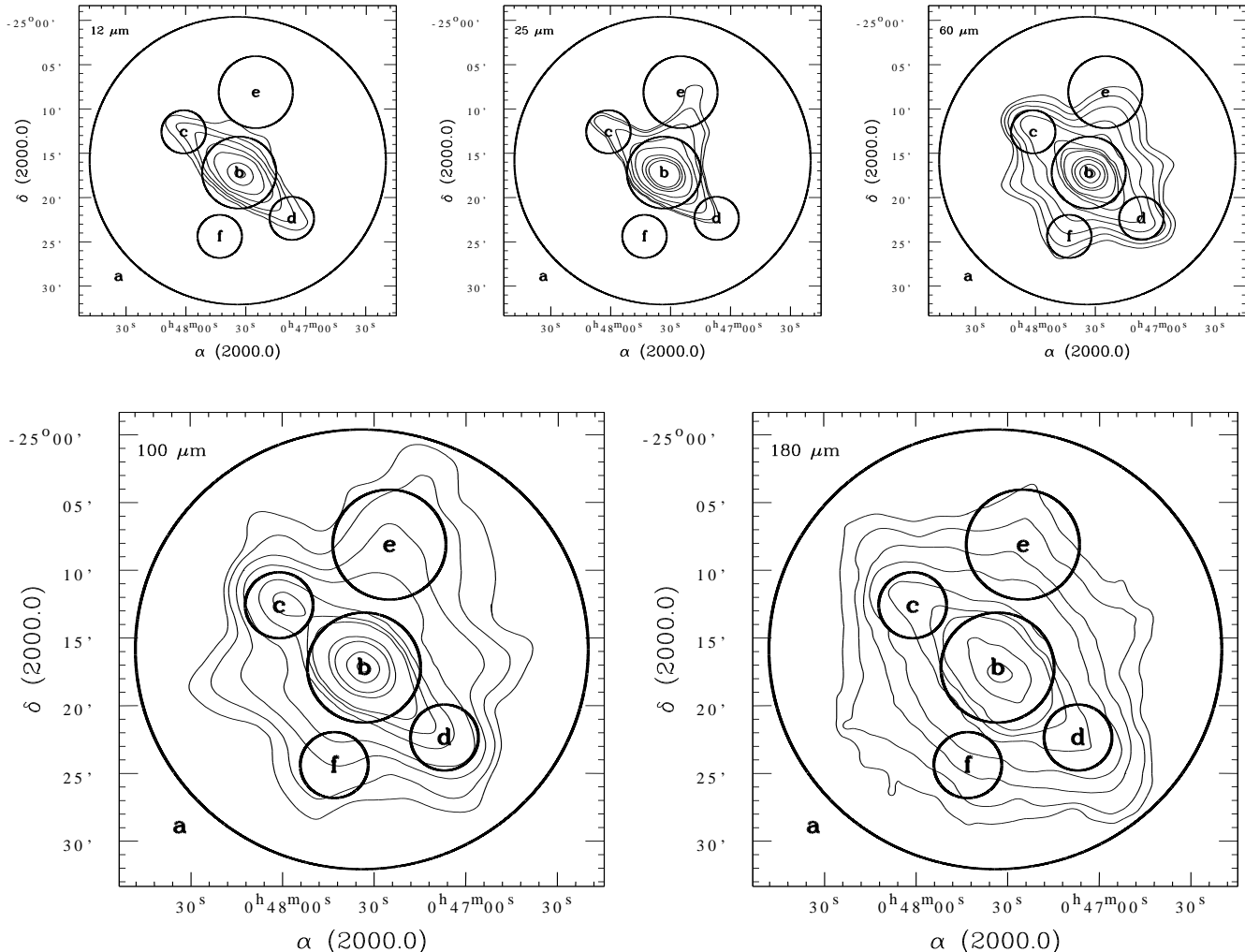


Fig. 3. Contour maps of the IRAS and ISOPHOT images and circular apertures where fluxes have been measured. The IRAS maps were transformed to the same position and resolution as the ISOPHOT map. The contour levels (MJy/sr) are: 12 μ m - 0.8, 1.5, 2.5, 5, 10, 30, 50, 80, 300, 500, 1000, 1500; 25 μ m - 1.2, 1.5, 2.5, 5, 10, 30, 50, 80, 300, 500, 1000, 1500; 60 μ m - 1.0, 1.5, 2.5, 5, 10, 30, 50, 80, 300, 500, 1000, 1500; 100 μ m - 1.5, 2.5, 5, 10, 30, 50, 80, 300, 500, 1000, 1500; 180 μ m - 1.5, 2.5, 5, 10, 30, 50, 80, 200, 300, 370.

two components in our data. We made an attempt to estimate the emission that would be produced by a ‘point-like’ source ($\text{FWHM} \leq 122''$); we shall define this component as the ‘nucleus’, with the understanding that actually it is the sum of nuclear and disk emission inside the region that would be seen as ‘point-like’ by the C200 detector. To this aim, we followed a procedure similar to that described by Alton et al. (1998a). We normalized the 2D beam profiles to the observed peak surface brightnesses and integrated them in an aperture of diameter $\sim 8'$. In the case of the IRAS images we used the beam maps provided by IPAC. In the case of ISOPHOT we used a 2D gaussian fit of the point-like source where the beam profile was measured: this was normalized to the peak surface brightness found in the 180 μ m strip map since the nucleus in the large 180 μ m map is saturated. The ratio of the IRAS total to nuclear (rescaled beam maps) fluxes gives results similar

to those found by Alton et al. (1998a) for infrared-bright galaxies, namely $F_{60}^{\text{tot}}/F_{60}^{\text{nuc}} \sim 1.4$ and $F_{100}^{\text{tot}}/F_{100}^{\text{nuc}} \sim 1.8$; from the ISOPHOT map we get $F_{180}^{\text{tot}}/F_{180}^{\text{nuc}} \sim 3$. It follows that while $\sim 70\%$ of the 60 μ m emission comes from the nucleus, emission at longer wavelengths is dominated by the outer regions.

In the halo component, fluxes from the IRAS maps may be affected in an unknown way by instrumental spurious effects, as seen above. As explained in www.ipac.caltech.edu/ipac/iras/iras_data_features.html, very bright (> 500 Jy) pointlike sources may produce a six-pointed star shape due to the reflection from the secondary mirror struts; there is no known method to remove this effect. Such a pattern is seen in the IRAS maps of NGC 253 at 60 μ m and 100 μ m (Fig. 3); however, we note that the same pattern in the ‘putative’ diffuse emission may be recognized not only in the ISOPHOT

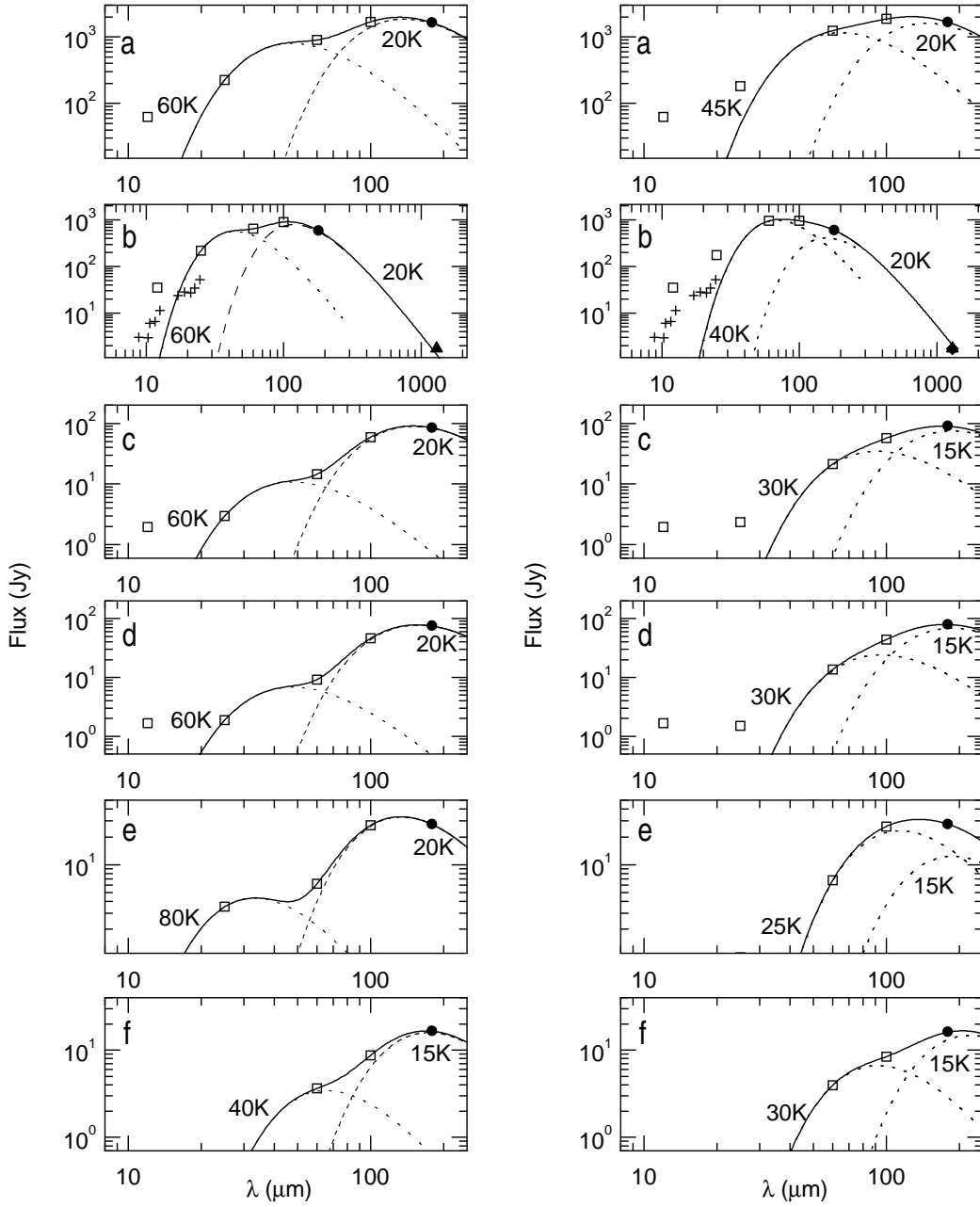


Fig. 4. Spectral energy distributions measured in the regions displayed in Fig. 3; fluxes have been color corrected. IRAS fluxes are displayed by squares, ISOPHOT fluxes by circles; crosses show ground-based photometry of the nucleus (5.5" aperture) taken from NED; the triangle is the $1300\mu\text{m}$ flux given by Krügel et al. (1990).

180 μm map, but also in the ROSAT images (see e.g.: Pietsch et al. 2000, panels B (0.1-2.4 keV) and S (0.1-0.4 keV) in their Fig.1; Forbes et al. 2000, Fig.2). We therefore conclude that the diffuse emission detected in the IRAS maps is probably real at $\lambda \geq 60\mu\text{m}$ and maybe at $25\mu\text{m}$, while no significant contribution is detected at $12\mu\text{m}$; since we cannot exclude the existence of instrumental effects, fluxes from low surface brightness regions in the IRAS maps should be considered as upper limits.

3.1. Spectral Energy Distributions

Physical quantities (dust temperatures and masses) in the different regions were first derived fitting the observed SED with modified blackbodies, i.e. blackbodies with a wavelength dependent emissivity (see e.g. Hildebrand 1983). Far-infrared fluxes in the observed range (12-180 μm) are probably due (Desert et al. 1990) to a mix of polyaromatic hydrocarbon molecules (PAHs), very small grains and big grains. Emission is dominated by PAHs at $12\mu\text{m}$, by cold silicate and graphite grains at $\lambda \geq 140\mu\text{m}$ (Dwek et al. 1997, Sturm et al. 2000, Genzel & Cesarsky

Table 2. Distances from nucleus (r) and diameters (d) of the apertures within which fluxes were measured; dust temperatures, infrared luminosities (1-1000 μm) and dust masses derived from the fits with and without the 25 μm point are displayed.

Total		Nucleus		Disk		Halo	
	a	b	c	d	e	f	
r [']	0	0	8	8	9	8	
r [kpc]	0	0	6	6	7	6	
d [']	33	8	5	5	8	5	
d [kpc]	24	6	4	4	6	4	
Observed fluxes, not color corrected							
12 μm	63.2	35.0	2.0	1.7	—	—	
25 μm	181	178	2.4	1.5	3.3	≤ 0.1	
60 μm	1186	853	19.1	12.2	6.1	3.6	
100 μm	1770	949	56.6	44.0	25.5	8.3	
180 μm	1693	607	87.3	77.4	28.3	15.7	
Fit from 25 μm to 180 μm							
Warm component							
T [K]	60	60	60	60	80	40	
L _{IR} [L_\odot]	1.07E+10	8.18E+09	1.44E+08	9.08E+07	8.32E+07	3.33E+07	
M _d [M_\odot]	7.42E+04	3.59E+04	1.04E+03	6.47E+02	6.75E+01	1.61E+03	
Cold component							
T [K]	20	20	20	20	20	15	
L _{IR} [L_\odot]	8.51E+09	4.24E+09	3.76E+08	3.14E+08	1.56E+08	5.80E+07	
M _d [M_\odot]	3.51E+07	7.23E+06	2.69E+06	2.79E+06	5.42E+05	9.84E+05	
Fit from 60 μm to 180 μm							
Warm component							
T [K]	47	39	28	27	25	29	
L _{IR} [L_\odot]	7.90E+09	5.76E+09	1.91E+08	1.27E+08	1.26E+08	4.60E+07	
M _d [M_\odot]	2.36E+05	5.47E+05	1.34E+05	1.05E+05	1.86E+05	2.32E+04	
Cold component							
T [K]	20	20	17	16	17	13	
L _{IR} [L_\odot]	7.72E+09	2.22E+09	2.51E+08	2.29E+08	4.40E+07	4.22E+07	
M _d [M_\odot]	3.83E+07	9.81E+06	3.88E+06	3.85E+06	6.74E+05	3.30E+06	

2000); at intermediate wavelengths each of the three components may contribute to the observed fluxes. Our purpose is to determine temperatures and masses of the cold dust component, but due to the limited number of points it is not possible to obtain a univoque fit (see Lisenfeld et al. 2000 for a discussion about the non uniqueness of single-temperature fits for the far-infrared SEDs). In order to estimate the impact of this uncertainty we first made a fit including all the points with the exception of the one at 12 μm , which is dominated by PAHs. The fit was then repeated dropping the 25 μm point, leading to lower dust temperatures and higher dust masses; values from this fit are indicated in italics.

We used for the fit the sum of two modified blackbodies and an emissivity $\propto \lambda^{-2}$. Color correction was applied according to the temperatures found and the whole procedure was repeated until convergence. The observed fluxes and fitted SEDs are shown in Table 2 and Fig. 4. For each component, we computed dust masses according to Klaas & Elsässer (1993), assuming dust grain properties as in Hildebrand (1983) for the emissivity adopted here :

$$M_d = 7.9 \times 10^{-5} (T_K/40)^{-6} L_{\text{IR}}/L_\odot [M_\odot], \quad (1)$$

where L_{IR} is the luminosity between 1 and 1000 μm computed from the extrapolation of the modified blackbodies.

Total fluxes from the whole galaxy (a) were computed from the integration in a circular aperture with 33' diameter. Fluxes from 25 to 180 μm are well fitted by a two-component blackbody with $T \sim 60(47)$ K and $T \sim 20$ K. Using the dust mass derived from the SED integrated over the whole galaxy ($M_d \sim 3.5(3.8) \times 10^7 M_\odot$) and the total mass ($M(\text{HI} + \text{H}_2) = 2.4 \times 10^9 M_\odot$) estimated by Houghton et al. (1997) we obtain a dust to gas mass ratio $\sim 1/70$, somewhat higher than the Galactic value (1/160).

1. *Nucleus* – The nuclear SED (b) is fitted by two components, a warm one ($T \sim 60(39)$ K) and a cold one ($T \sim 20$ K). The ratio of the extrapolated 1-1000 μm luminosities in the two components is $L_w/L_c \sim 2$, i.e. the emission is dominated by the warm component. We estimate a dust mass $\sim 7(10) \times 10^6 M_\odot$. In order to check the reliability of the separation of the ‘nuclear’ emission from the extended emission, we extrapolated the nuclear SED to 1300 μm and compared it with the flux given by Krügel et al. (1990), 1.7 Jy in an area of

$3' \times 2'$: the two values agree within 30(8)%, which is acceptable considering the uncertainties involved.

2. *Disk* – The SEDs in the NE (*c*) and SW (*d*) regions of the disk show, as in the nucleus, the presence of a warm ($T \sim 60(28)$ K) and a cold ($T \sim 20(17)$ K) component. However, emission is dominated by the cold component, $L_w/L_c \sim 0.3(0.5)$. The dust mass estimated in each of these regions is $\sim 3(4) \times 10^6 M_\odot$.

3. *Halo* – Due to the uncertainty in the IRAS fluxes, a SED decomposition is very difficult; the results given here are therefore indicative. In the southern halo (*f*) we could only assume an upper limit for the flux at $25 \mu\text{m}$ since no significant emission was detected. Dust temperatures of the cold component are similar to those found in the disk, $T \sim 20(17)$ K, with a somewhat lower temperature in the southern halo (*f*) where $T \sim 15(13)$ K; we derive dust masses in the order of $0.5\text{--}1(0.7\text{--}3) \times 10^6 M_\odot$. In order to explain the non detection by IRAS of emission by dust involved in outflows, Alton et al. (1998a) argued that the temperature of the dust is $T \sim 15\text{--}20$ K and its mass $< (0.5\text{--}3.5) \times 10^5 M_\odot$: this limit is not far from the values we find for NGC 253, in particular if we consider that if $T \sim 20$ K an uncertainty in the temperature of $\Delta T = 5$ K may change the dust mass by a factor of 5. For comparison, Phillips (1993) gave a dust mass of $2 \times 10^5 M_\odot$ for the outflow in NGC 1808; Alton et al. (1999) estimated for the outflow in M82 dust masses of $10^6\text{--}10^7 M_\odot$.

According to Kennicutt (1998), the star formation rate for continuous bursts of age 10–100 Myr in starbursts, where contribution of dust heating from old stars may be neglected, is:

$$\text{SFR} = 1.7 \times 10^{-10} L_{\text{IR}}/L_\odot [M_\odot \text{ yr}^{-1}] \quad (2)$$

The SFR obtained in the nucleus and in the whole galaxy is $\sim 2.1(1.3)$ and $3.3(2.6) M_\odot \text{ yr}^{-1}$, respectively. This low value of the SFR is in agreement with the conclusion by Engelbracht et al. (1998) that NGC 253 is in a late phase of the starburst, having passed a rapid decrease of the star formation rate.

4. Modeling the FIR emission

The far-infrared emission of NGC 253 was modeled with a Monte Carlo simulation system (Kahanpää 2001, in preparation) using both the $180 \mu\text{m}$ map for FIR major and minor axis profiles and the strip maps at 0, 10 and $15'$ for minor axis profiles and photometry at 120 and $180 \mu\text{m}$.

4.1. The galaxy model

The galaxy model is based on a cylindrically symmetrical disk with exponential distributions along the radius and height with an additional, compact nuclear energy source. The distribution of stars within the disk was assumed to

be independent of wavelength; no intrinsic color gradients in the stellar population were taken into account. While this ignores color gradients due to the bulge, the impact on the resulting FIR colors is minor as NGC 253 is a disk-dominated spiral (Baggett et al. 1998). The core was treated as an independent source with its own unobscured spectral energy distribution. Since recent studies by Davies et al. (1999) suggest that the scale lengths of star and dust populations are not equal, the scale lengths were treated as independent parameters in the model.

4.2. Radiative transfer code

Unlike most radiative transfer codes our model does not ignore the cloud structure of the interstellar medium (ISM). Instead, all dust is in clouds; the total number of clouds is determined by the total dust mass and the cloud positions are randomly chosen from a double-exponential distribution:

$$R_1 = \frac{\int_0^r ue^{-u/r_0} du}{\int_0^{r_{\text{max}}} ue^{-u/r_0} du}, \quad (3)$$

$$R_2 = \frac{\int_{-z_{\text{max}}}^z e^{-u/z_0} du}{\int_{-z_{\text{max}}}^{z_{\text{max}}} e^{-u/z_0} du}, \quad (4)$$

where R_1 and R_2 are uniform random numbers and r_0 and z_0 the dust scale length and scale height respectively.

The radiative transfer code for the optical domain is based on models by de Jong (1996) and Bianchi et al. (1996). The assumed unobscured spectral energy distribution of the energy sources (stars) was divided into a number of energy bins – each formally representing one broad-band filter – and the radiative transfer problem was numerically solved for each bin by following numerous simulated photons through the dust system. For each bin $2 \cdot 10^5$ to $1 \cdot 10^6$ random paths through the dusty layer were calculated; the total number of independent paths used in a single model was typically $40 \cdot 10^6$. The resulting surface brightness distribution for each wavelength was recorded. Additionally the cumulative amount of absorbed energy at each position within the model galaxy was registered for further processing. When all bins had been processed, the equilibrium temperature of individual dust grains as a function of grain size and position within the galaxy (distance from the nucleus and height above the plane of the galaxy) was solved. In thermal equilibrium the emitted power from a single grain is

$$P_{\text{em}} = \int_0^\infty 4\pi^2 a^2 Q_{\text{abs}}(\lambda, a) B(\lambda, T) d\lambda, \quad (5)$$

where a is the grain radius, Q_{abs} is the absorption coefficient of the grain and B is the blackbody (Planck) function. The shape of Q_{abs} in the FIR was approximated with

$$Q_{\text{abs}}(a, \lambda) = 1.8 \times 10^{-4} a \lambda^{-\beta}. \quad (6)$$

We have used $\beta = 2$, a typical value for grain temperatures less than 50 K, and dust grain size distributions and optical properties from Désert et al. (1990).

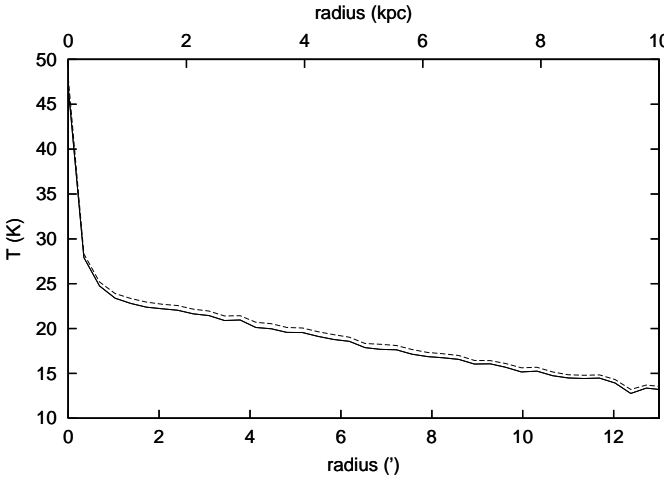


Fig. 5. Grain temperature in the galactic plane of NGC 253. The solid line represents grains with a diameter of 150 nm, the dotted line the smallest classical grains in the model ($d = 15$ nm).

The dust model chosen is of secondary importance; we tried using the classical MRN dust population models with $n(a) \propto a^{-3.5}$ (Mathis et al. 1977) and got the same results for classical dust emission. Infrared emission from very small grains and PAHs with stochastic heating and cooling processes were neglected as they are minor contributors in the 100-200 μm wavelength range studied here; they were, however, still included as absorbers with size distributions and optical properties as given by Désert et al. (1990).

4.3. Model input parameters

Table 3 summarizes the parameter values used in the model. The observed total stellar fluxes as a function of wavelength were obtained from the NASA-IPAC extragalactic database (NED). The radial scale length of the stellar component was obtained by comparing the resulting brightness profiles for the optically thin outer parts of the axial profiles with published measurements of the major and minor axis profiles in the B and V bands (Pence 1980, Baggett et al. 1998). As a byproduct the inclination of NGC 253 was found to be $78^\circ \pm 1^\circ$. Limiting values for the radial dust scale length were found by comparing the model results with the observed major axis profile at 180 μm . Since the model profile depends also on the temperature of the dust grains, this fit does not give as stringent limits as in the optical case, but if the scale length was varied by more than 15%, the fit was unacceptably poor. The major parameters of the model were adjusted until a reasonable fit to the optical and FIR data was found. Unobscured SEDs for the disk and nucleus components were approximated with model SEDs for stellar populations (Silva 1998). For the core we used a 200-My old population without modifications; in the disk a combination of young (0.2 Gy) and old (5 Gy) populations

Table 3. Model input parameters and results for NGC 253

Input parameters	
Distance	2.5 Mpc
Stars, luminosity	$3.2 \times 10^{10} \text{ L}_\odot$
Stars, core to disk luminosity ratio	0.5
Dust, cloud size	40 pc
Dust, grain density	3 g cm^{-3}
Dust, maximum albedo	0.7
Dust, size distribution	As in Désert et al. 1990
Results	
Inclination	78°
Stars, scale length	1.8 kpc
Stars, scale height	0.2 kpc
Dust, scale length	2.8 kpc
Dust, scale height	0.15 kpc
Dust, total mass	$2.8 \times 10^7 M_\odot$
τ_V (center)	4.5 ± 0.5
FIR luminosity	$1.7 \times 10^{10} \text{ L}_\odot$
Large grain Lumin.	$1.2 \times 10^{10} \text{ L}_\odot$
VSG & PAH Lumin.	$0.45 \times 10^{10} \text{ L}_\odot$
$T(r=0.5 \text{ kpc})$	$25 \pm 1 \text{ K}$
dT/dr in disk	1.2 K kpc^{-1} (1-10 kpc)

was required. The resulting unobscured SED is shown in Fig. 6.

4.4. Predicted dust mass, distribution and temperature profiles

According to the computed model the face-on optical depth of the dust layer at the center of the galaxy is 4.5 at 550 nm. After the inclination of NGC 253 (78°) is taken into account this makes the core attenuated by roughly 11 magnitudes in the V band. Values based on earlier observations are somewhat higher: Engelbracht et al. (1998) estimated $A_V(\text{cen}) = 19.07 \pm 3.3$ from the H-K excess, but as the small starburst core certainly includes a sizeable amount of hot local and circumstellar dust, this is to be expected. Half (54%) of the total model luminosity ($3.2 \times 10^{10} \text{ L}_\odot$) is converted to FIR emission by the dust grains. The total mass of the cold dust component as inferred from the model is $M \sim 0.93 \times 10^7 \rho_d M_\odot$, where ρ_d is the average density of the dust grains in units of g cm^{-3} . Using the value ($\rho_d = 3 \text{ g cm}^{-3}$) given by Hildebrand (1983) sets the dust mass of the model to $2.8 \times 10^7 M_\odot$, a value not too far from the estimate found by using Eq. 1.

A disk-to-nucleus luminosity ratio of 2.0 gave the best match with the observed SED and also results in a core luminosity $L_{\text{core}} = 1.1 \times 10^{10} \text{ L}_\odot$; the same value was found by Engelbracht et al. (1998) from a combination of mid- and far-infrared, sub-millimeter and 1.3 mm data.

Fig. 5 shows the radial temperature distribution of dust in the plane of NGC 253. The smallest grains tend to

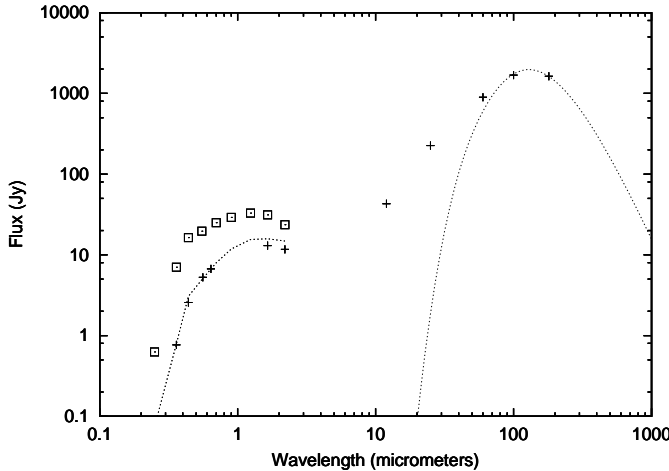


Fig. 6. Spectral energy distribution of NGC 253 in the optical-near infrared (ground-based photometry from NED) and far-infrared (IRAS 100 μm and ISOPHOT 180 μm fluxes). Crosses – observed SED; squares – unobscured SED; dashed line – model fit for the emission from stars and cold dust, as described in Sect. 4. IRAS fluxes from 12 to 60 μm were ignored in the fit since the model does not include the IR emission from PAHs or very small grains, which are responsible for most of the emission at these wavelengths.

be hotter and thus more efficient FIR emitters than their bigger companions because the FIR absorption coefficient of the grains at a given wavelength is proportional to grain diameter (see Draine & Lee 1984). This effect is partially counterbalanced by the spectral shape of the attenuated interstellar radiation field (ISRF) within the galaxy: the smallest grains are poor absorbers in the near infrared, where the ISRF is most intense.

The central dust temperature given by the model of NGC 253 is higher than that given by a simple fit to the FIR spectrum (Fig. 4). The central spectrum is, however, integrated over quite a large area and in the end the fit is sufficiently good. The hot central core is very small and its contribution to the total SED is approximately 40% of the total luminosity. The total SED (Fig. 6) as well as the strip map flux levels at 120 and 180 μm at 0' and 10' are perfectly reproduced.

The derived scale lengths of the stellar and dust components are 1.8 and 2.8 kiloparsecs respectively. As the uncertainty of both values is of the order of 15%, the difference is significant. This agrees with the recent observations of dust distribution in other nearby spiral galaxies (Alton et al. 1998b, Alton et al. 2001). A prominent effect of the difference in the scale lengths is the variation of the dust to stellar mass ratio with radius: at 10 kpc the relative dust density is four times as large as at the center.

The halo dust component cannot be reproduced by a single 3-D exponential dust disk: the modeled minor axis profiles (convolved to 120" FWHM) are narrower than the observed profiles of NCG 253 at 120 and 180 μm .

This can be due to several different effects or a combination of them:

1. There is an extra source heating the halo, which is not represented by the stellar populations in the model.
2. A halo population of young stellar objects (YSO) or other compact FIR emitters is present in NGC 253.
3. The dust distribution in the halo has a distribution which significantly deviates from a simple exponential model.

The two first scenarios are in agreement with the existence of star formation in the halo of NGC 253, which has been recently proposed by Comerón et al. (2001) on the basis of UBV photometry. In this case we should be able to see the optical emission of the heating sources as the halo is certainly optically thin. The very cold spectrum of the outer parts contradicts the second case as YSO sources usually have SED with strong near and mid-infrared components. In the third case, which we find most probable, the excess dust in the halo is heated by stars in the disk of NCG 253. If a dust halo is the most important contributor it should also be observable in the optical domain as a faint, blue halo of scattered light.

5. Conclusions

ISOPHOT observations were used together with IRAS data to map the far-infrared emission in the starburst galaxy NGC 253. The resulting images were then analyzed with modified blackbody fits as well as radiative transfer modeling. The total FIR luminosity consists of two parts: a warm component ($T \sim 47\text{--}60$ K), dominated by the central regions, and a cold component ($T \sim 20$ K) produced in the disk and the halo. Dust temperatures and masses derived from single-temperature fits of the SED integrated over the whole galaxy are in agreement with those obtained by solving the radiative transfer equations. The results obtained in the different regions may be summarized as follows:

Nucleus: the nucleus produces half of the total FIR luminosity of NGC 253. Our fit for the core correctly predicts the observed 1.3 mm continuum emission given by Krügel et al. (1990). The low inferred star formation rates suggest that the nuclear starburst in NGC 253 is in a late phase, having passed a rapid decrease of the star formation rate.

Disk: the resulting dust temperatures are typical for the general diffuse ISM in spiral galaxies. The radiative transfer model indicates that the dust scale length is $\sim 40\%$ larger than that of stars; the same trend was found by Alton et al. (1998b). The dust is warmer ($T > 20\text{K}$) in the central regions of the galaxy, the outer regions are dominated by colder dust ($T \leq 15\text{K}$).

Halo: we find evidence for extended emission to projected distances of ~ 10 kpc from the nucleus along the minor axis both in the IRAS and ISOPHOT maps; the emission seen in the IRAS maps could be due to instrumental effects, but since the same emission pattern is also

seen in the ISOPHOT map as well as in ROSAT images (e.g. Pietsch et al. 2000, Forbes et al. 2000) we conclude that this is not the case. The SED fitting of this extended component is very uncertain, since IRAS fluxes *may still be affected by instrumental effects*. Keeping in mind this uncertainty, the emission is probably dominated by cold dust ($T \sim 15 - 20$ K); the derived dust masses are comparable to those found for the outflows in NGC 1808 and M 82. The apparently constant mass in the outflows observed in nearby galaxies is probably due to limitations in the instrumental resolution and sensitivity. It was not possible to reproduce the halo component by a single 3-D exponential dust disk. Even if in our opinion this is most likely due to a non exponential distribution of dust in the halo, some extra heating may be given by star formation, which according to Comerón et al. (2001) may occur in the halo. Both phenomena may be related to the interaction of the interstellar medium with the superwind driven by the nuclear starburst.

Acknowledgements. The ISOPHOT development and the post-operation phase performed in the ISOPHOT Data Centre at the Max-Planck-Institut für Astronomie Heidelberg are supported by Deutsches Zentrum für Luft- und Raumfahrt (DLR), Bonn. The authors are responsible for the content of this paper. PIA has been jointly developed by the ESA Astrophysics Division and the ISOPHOT consortium. We are grateful to the referee for the useful comments which improved this paper. We are indebted to Manfred Stickel of the Heidelberg ISOPHOT Data Center for having provided his procedures. We thank IPAC for the IRAS HIRES maps. This research has made use of the NASA-IPAC extragalactic database (NED) which is operated by the Jet Propulsion Laboratory, Caltech, under contract with the NASA.

References

Alton, P.B., Davies, J.I. & Bianchi, S. 1999, A&A, 343, 51
 Alton, P.B., Davies, J.I. & Trewella, M. 1998a, MNRAS, 296, 773
 Alton, P.B., Lequeux, J., Bianchi, S., et al. 2001, A&A, 366, 451
 Alton, P.B., Trewella, M., Davies, J.I., et al. 1998b, A&A, 335, 807
 Baggett, W.E., Baggett, S.M. & Anderson, K.S.J. 1998, AJ, 116, 1626
 Bianchi, S., Ferrara, A. & Giovanardi, C. 1996, ApJ, 465, 127
 Chevalier, R.A. & Clegg, A.W. 1985, Nature, 317, 44
 Comerón, F., Torra, J., Mèndez, R.A. & Gòmez A.E. 2001, A&A, 366, 796
 Dahlem, M., Weaver, K.A. & Heckman, T.M. 1998, ApJS, 118, 401
 Davies, J.I., Alton, P., Trewella, M., et al. 1999, MNRAS, 304, 495
 de Jong, R.S. 1996, A&A, 313, 377
 Désert, F.-X., Boulanger, F. & Puget, J.L. 1990, A&A, 237, 215
 de Vaucouleurs, G., de Vaucouleurs, A., Corwin, H.G., et al. 1991, Third Reference Catalogue of Bright Galaxies (ed. Springer Verlag)
 Draine, B.T. & Lee, H.M. 1984, ApJ, 285, 89
 Dudley, C.C. & Wynn-Williams, C.G. 1999, MNRAS, 304, 549
 Dwek, E., Arendt, R.G., Fixsen, D.J., et al. 1997, ApJ, 475, 565
 Engelbracht, C.W., Rieke, M.J., Rieke, G.H., et al. 1998, ApJ, 505, 639
 Fabbiano, G. 1988, ApJ, 330, 672
 Forbes, D.A., Polehampton, E., Stevens, I.R., et al. 2000, MNRAS, 312, 689
 Fruchter, A.S. & Hook, R.N. 1997, in Applications of Digital Image Processing XX, Proc SPIE, Vol. 3164, ed. A. Tescher
 Genzel, R. & Cesarsky C.J. 2000, ARA&A, 38, 761
 Heckman, T.M., Armus, L. & Miley, G.K. 1990, ApJS, 74, 833
 Hildebrand, R.H. 1983, QJRAS, 24, 267
 Houghton, S., Whiteoak, J.B., Koribalski, B. et al. 1997, A&A, 325, 923
 Kennicutt, R.C. 1998, ARA&A, 36, 189
 Kessler, M.F., Steinz, J.A., Anderegg, M.E., et al. 1996, A&A, 315, L27
 Klaas, U. & Elsässer, H. 1993, A&A, 280, 76
 Klaas, U., Krüger, H., Heinrichsen, I., et al. 1994, ISOPHOT Observer's Manual, Version 3.1 (Noordwijk: ESA), ISO Explanatory Library, http://www.iso.vilspa.esa.es/manuals/iso_pht/om311.html
 Klaas, U., Laureijs R.J., Radovich M., et al. 2000, ISOPHOT Calibration Accuracies, Version 4.0, SAI/1998-092/Dc, http://www.iso.vilspa.esa.es/manuals/users/expl_lib/PHT/calacc.v4.ps.gz
 Krügel, E., Chini, R., Klein, U., et al. 1990, A&A, 240, 232
 Laureijs, R.J., Klaas, U., Richards P. & Schulz, B. 1998, ISOPHOT Data Users Manual, V 4.0, ISO Explanatory Library, SAI/95-220/Dc, http://www.iso.vilspa.esa.es/manuals/pht_idum4/
 Lemke, D., Klaas, U., Abolins, J., et al. 1996, A&A, 315, L64
 Mathis, J.S., Rumpl, W., Nordsieck, K.H. 1997, ApJ, 217, 425
 Lisenfeld, U., Isaak, K.G. & Hills, R. 2000, MNRAS, 312, 433
 McCarthy, P.J., Heckman, T. & van Breugel, W. 1987, AJ, 92, 264
 Pence, W.D.S. 1980, ApJ, 239, 54
 Phillips, A.C. 1993, AJ, 105, 486
 Pietsch, W., Vogler, A., Klein, U. & Zinnecker, H. 2000, A&A, 360, 24
 Rice, W. 1993, AJ, 105, 67
 Silva, L., Granato, G.L., Bressan, A., et al. 1998, ApJ, 509, 103
 Sturm, E., Lutz, D., Tran, D., et al. 2000, A&A, 358, 481
 Trewella, M., Davies, J.I., Alton, P.B., et al. 2000, ApJ, 543, 153